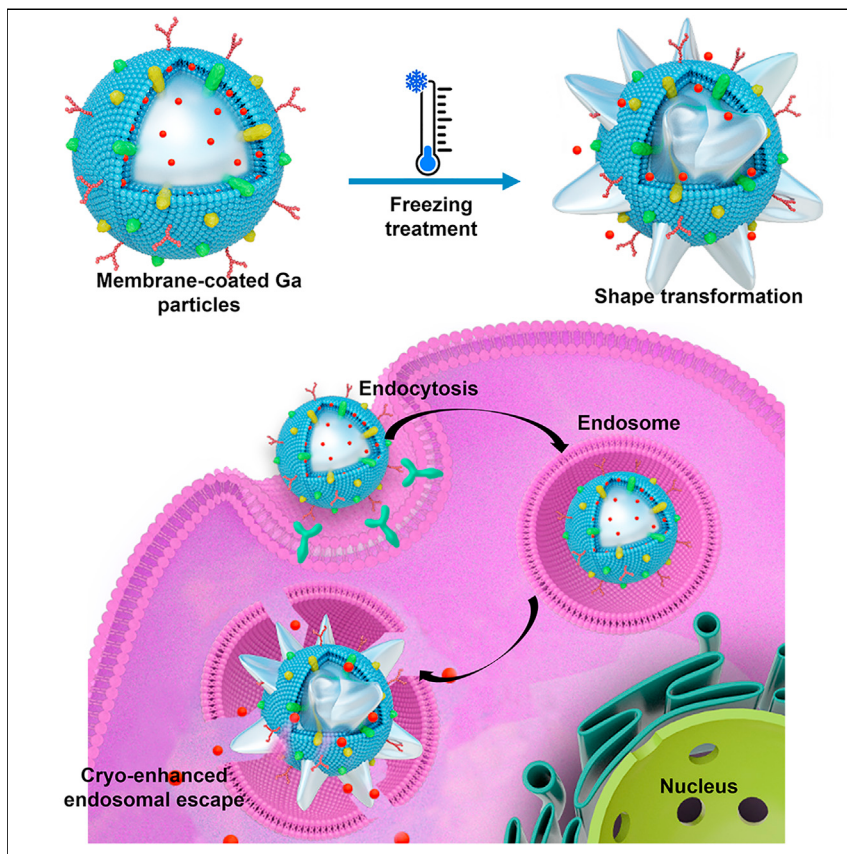


## Article

# Endosomal escapable cryo-treatment-driven membrane-encapsulated Ga liquid-metal transformer to facilitate intracellular therapy



A key challenge that remains in metallic shape transformable materials is to achieve controllable morphological transformation in biomedical applications. We find that Ga particles with cell membrane encapsulation (Ga/MPs) exhibit distinct shape variation from sphere shape to cactus-like structure under cryo exposure. Ga/MPs exhibit remarkable tumor growth inhibition in *in vivo* tumor treatments with efficient endosomal escape. This strategy provides huge potential for Ga-based liquid metal as novel shape transformable materials to improve tumor therapeutic effect in intracellular tumor cryotherapy.

### Demonstrate

Proof-of-concept of performance with intended application/response

4

Xuelin Wang, Xuedong Li,  
Minghui Duan, ..., Liang Hu,  
Junge Chen, Jing Liu

chenjg19@buaa.edu.cn (J.C.)  
jliubme@mail.tsinghua.edu.cn (J.L.)

### Highlights

Freezing drives Ga particles to transform from sphere to cactus-like structure

LM transformers can realize endosomal escape for drug release under freezing

Ga/MPs exhibit significant tumor growth inhibition and prolonged survival time

LM transformers can be applied for high-resolution *in vivo* CT imaging

Wang et al., Matter 5, 219–236  
January 5, 2022 © 2021 Elsevier Inc.  
<https://doi.org/10.1016/j.matt.2021.11.006>



## Article

# Endosomal escapable cryo-treatment-driven membrane-encapsulated Ga liquid-metal transformer to facilitate intracellular therapy

Xuelin Wang,<sup>1</sup> Xuedong Li,<sup>2</sup> Minghui Duan,<sup>3</sup> Shaobo Shan,<sup>1</sup> Xiyu Zhu,<sup>3</sup> Yi Chai,<sup>4</sup> Hongzhang Wang,<sup>3</sup> Xuyang Sun,<sup>1</sup> Lei Sheng,<sup>5</sup> Guangchao Qing,<sup>6</sup> Wei Rao,<sup>5</sup> Liang Hu,<sup>1</sup> Junge Chen,<sup>1,\*</sup> and Jing Liu<sup>3,5,7,\*</sup>

## SUMMARY

Metallic shape transformable materials hold big promise for improved intracellular therapy. However, until now, there have been rather limited biomedical practices for such materials, which is mainly attributed to their inherent uncontrolled morphological transformation, non-selective destruction, and difficult metabolization. Here, Ga-based liquid metal is found to exhibit remarkable transformation from sphere shape to cactus-like structure in micro-scale under freezing. Particularly, only cell membrane-encapsulated Ga particles (Ga/MPs) display dramatic shape variation in cooling under cryo-transmission electron microscopy (cryo-TEM). Following that, cryo-triggered Ga/MPs transformers are designed for effective endosomal escape via a physical mechanical strategy to disrupt the endosomal membrane, which leads to highly efficient cancer cell killing. Ga/MPs exhibit significant tumor growth inhibition and prolonged survival time according to the collaborative efficacy of cryoablation and endosomal escape mechanism, as well as high-resolution *in vivo* computed tomography (CT) imaging. This study opens a versatile strategy based on Ga particle transformer to assist high-performance precise intracellular therapy in future tumor therapeutics.

## INTRODUCTION

Due to attractive electrical and thermal conductivities, malleable and ductile mechanical properties, and biocompatibility, Ga-based liquid-metal (LM) materials have recently received prominent advances in a wide range of areas,<sup>1,2</sup> such as flexible electronics,<sup>3–5</sup> health monitoring,<sup>6–8</sup> artificial bone substitute,<sup>9</sup> *in vivo* imaging,<sup>10,11</sup> and disease treatment.<sup>12–14</sup> Mesoscale LMs with external stimulations have achieved remarkable shape changes with efficient manipulations, which are considered as large-scale LM transformers.<sup>15,16</sup> The external stimulations mainly include electric field, magnetic field, light, heat, mechanical force, and chemical and electrochemical stimuli.<sup>15–17</sup> An electrical field stimulus causes LM to transform from an original flattened state to a sphere.<sup>18</sup> Magnetic field is an important external stimulation for large-scale LM transformers with transformer shape and reconfigurable polarity.<sup>19</sup> Large-magnitude LM composites display controllable shape change from 2D shape into 3D shape when subjected to heating.<sup>17,20</sup> Chemical-electrical stimulus can control LM with a large-scale reversible deformation between droplet and asymmetric structure.<sup>21</sup> Mixing magnetic iron particles into LM enables LM to undergo certain phase changes.<sup>22</sup> Chemical solutions such as CuSO<sub>4</sub> solution can induce LM surface tension change and therefore drive self-growing LM to different

## Progress and potential

This study presents a novel cryo-facilitated liquid-metal (LM) particles transformer with physical mechanical destruction to endosomal membrane for endosomal escape and drug release to enhance antitumor cryotherapy efficacy and using a freezing stimulus for the LM transformation. Remarkable morphological transformation of cell membrane-coated Ga particles (Ga/MPs) is discovered in the cryogenic environment from sphere structure to cactus-like structure under cryo-transmission electron microscopy (cryo-TEM) observation. For killing the cancer cells efficiently, the obtained cryo-triggered Ga/MP transformers are specially designed via a physical mechanical procedure to disrupt the endosomal membrane so that effective endosomal escape is possible. In *in vivo* antitumor treatments settings, Ga/MPs have exhibited remarkable tumor growth inhibition and prolonged survival time. This study proposes a versatile strategy based on Ga particle transformers to assist high-performance precise intracellular therapy in future cancer therapeutic practices.



morphologies.<sup>23</sup> The implications of transformability of LM have contributed to many advancements in various fields, including soft machines, robotics, smart materials, biomimetic transformers, and remote operation.<sup>24,25</sup>

In contrast to these large-scale LM transformations, which are observed by the naked eye, micro-/nano-scaled LM particle transformations are challenging to study clearly, especially after different modification methods.<sup>16,26</sup> With the aid of an electron microscope, an oxide layer wrapping LM with a core-shell structure formation that provides relative stability for LM nanoparticles was observed.<sup>27,28</sup> Until now, the Ga-based particles have appeared to have reliable biosafety according to low cell toxicity in *in vitro* experiments and slow degradation in *in vivo* tumor environments, and thus are appropriate for biomedical applications.<sup>1,29</sup> Interestingly, increasing evidence has demonstrated that LM particles can represent corresponding stimuli-responsive properties under external stimulus conditions, including electric field, magnetic field, heat, and light.<sup>16,26,30</sup> For example, acidic environment triggers LM particles shape change with fusible and degradable behavior to become transformable LM nano-medicines.<sup>31</sup> Light can also fuel LM particles as nano-transformers from spherical nanostructure to rod-shaped nanostructure with a certain light exposure time.<sup>32</sup> All these novel findings indicate that external stimuli can induce LM particles' morphological change in micro/nano scale and therefore can be operated as new-generated micro-/nano-transformers. However, the corresponding conditions for the above stimuli are relatively difficult to control and it is also difficult to capture LM particle deformation. Consequently, a demand arose to explore new types of manageable and measurable stimulus methods to drive LM micro-/nano-transformer deformation.

Our previous research had shown that LM particles around 200 μm could puncture cells via a freezing-mediated deformation and resulted bomb-explosion-like mechanical destruction.<sup>33</sup> However, the LM micro-particles could not enter tumor cells because of their large size. More importantly, the damage mechanism was only the mechanical force piercing the cell membrane, without destroying the cells as a whole, and thus tumor recurrence could happen. Recently, nanocarriers have attracted much attention in tumor diagnosis and treatment intracellularly via the endosome-lysosome pathway after being endocytosed.<sup>34,35</sup> However, the acidic environment and a large number of enzymes in the endosome cause the degradation and destruction of nanocarriers, which lead to the inactivation of the loaded drugs inside nanocarriers. Hence, it is necessary that drugs quickly escape from endosome.<sup>36–39</sup> At present, the most demonstrated endosomal escape approaches with proton sponge effect strategy and lysosomal destroyers have shown difficult metabolism, accumulated toxicity, and non-selective destruction.<sup>40–42</sup> Recently, bioengineering methods based on cancer cell membranes have attracted much attention since Zhang and colleagues first reported their homotypic binding and immune escape functions.<sup>43,44</sup> The self-recognition function of biomimetic particles mainly relies on the interaction between natural membrane proteins and target cells to avoid the restriction of receptor expression density changes.<sup>45,46</sup> Bionic technology based on cancer cell membranes has been applied to tumor therapeutics,<sup>47,48</sup> molecular imaging,<sup>49</sup> and immunotherapy.<sup>44</sup> However, as far as we know, biomimetic particles for active targeting of melanoma cryotherapy are rarely reported.

On account of LM transformation triggered by freezing stimulus, we have hypothesized that if LM particles' morphological transformation occurred intracellularly, it could physically disrupt the endosomal membrane to facilitate endosomal escape with efficient cell-destroying effect. Remarkable morphological transformation of

<sup>1</sup>Beijing Advanced Innovation Center for Biomedical Engineering, Beijing Advanced Innovation Center for Big Data-Based Precision Medicine, School of Engineering Medicine, Beihang University, Beijing 100083, China

<sup>2</sup>Hygea Medical Technology Co., Ltd, Beijing 100089, China

<sup>3</sup>School of Medicine, Tsinghua University, Beijing 100084, China

<sup>4</sup>Department of Neurosurgery, Renji Hospital, School of Medicine, Shanghai Jiaotong University, No. 160, Pujian Road, District Pudong, Shanghai 200127, China

<sup>5</sup>Beijing Key Laboratory of Cryo-biomedical Engineering and CAS Key Laboratory of Cryogenics, Technical Institute of Physics and Chemistry, Chinese Academy of Sciences, Beijing 100190, China

<sup>6</sup>CAS Center for Excellence in Nanoscience, CAS Key Laboratory for Biomedical Effects of Nanomaterials and Nanosafety, Chinese Academy of Sciences, National Center for Nanoscience and Technology of China, Beijing, 100190, China

<sup>7</sup>Lead contact

\*Correspondence: chenjg19@buaa.edu.cn (J.C.), jliubme@mail.tsinghua.edu.cn (J.L.)

<https://doi.org/10.1016/j.matt.2021.11.006>

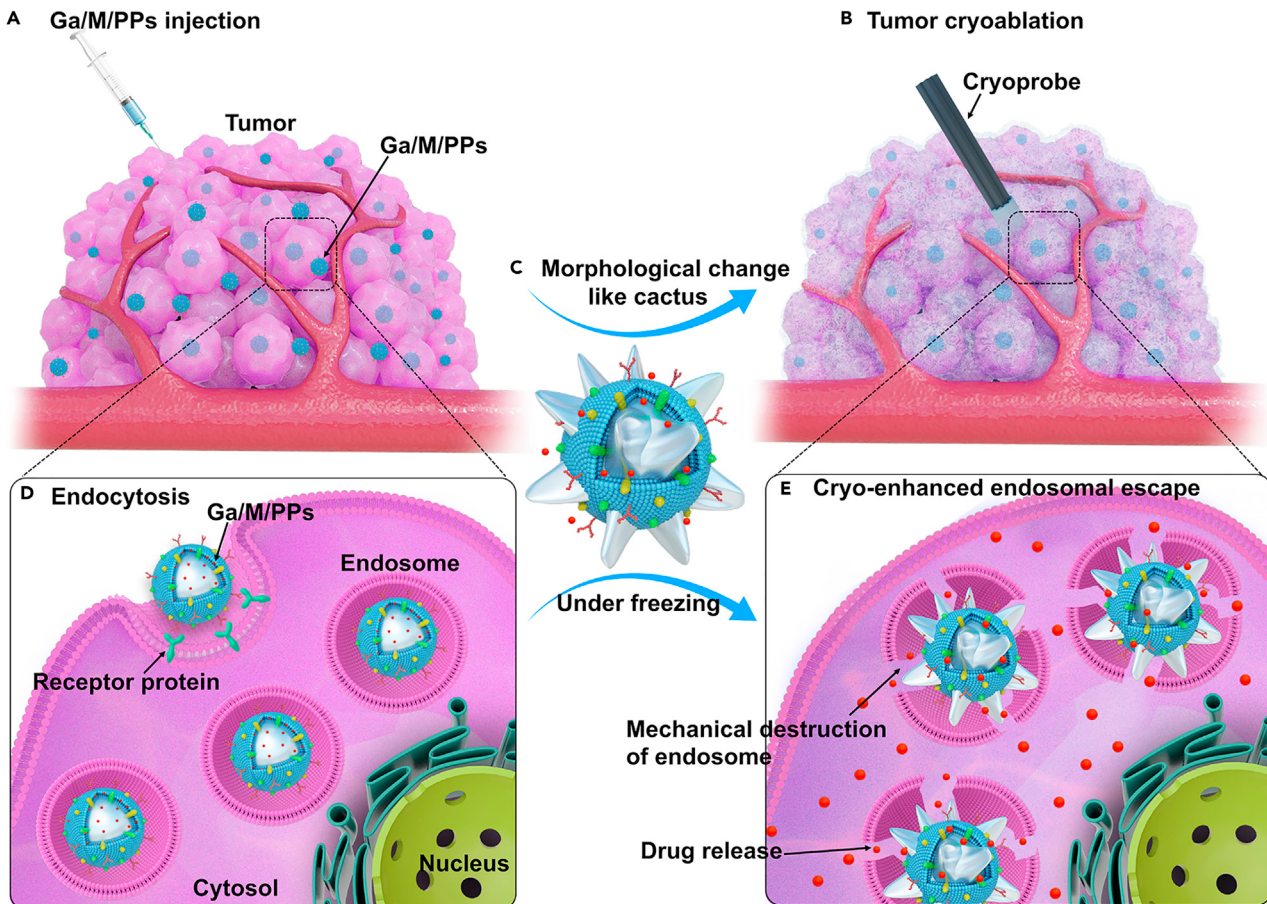


**Figure 1. Schematic illustration of cryo-facilitated LM particle transformation for endosomal escape**

- (A) Injection of Ga/M/PP solution into tumor tissue.
- (B) Endocytosis process of Ga/M/PPs in tumor cell.
- (C) Morphological change of Ga/M/PPs like cactus under freezing.
- (D) Tumor cryoablation process with cryoprobe inserting for antitumor therapy.
- (E) Cryo-enhanced endosomal escape caused by Ga/M/PPs' mechanical destruction of endosome to realize drug release and cell death.

cell membrane-coated Ga particles is discovered in cryogenic environments from sphere structure to cactus-like structure under cryo-transmission electron microscopy (cryo-TEM) observation. Dramatic shape deformation of cell membrane-coated Ga particles (GaPs) (Ga/MPs) with volume expansion during the phase transition process can directly puncture the endosome membrane, thus improving the probability of intracellular destruction. In addition, if the antitumor drug paclitaxel (PTX) is carried with Ga/MPs (PTX-loaded Ga/MPs: Ga/M/PPs), it can be released with endosome disruption under freezing stimulation to achieve efficient drug delivery as well. After injecting Ga/M/PPs at the tumor site, particles are endocytosed into the endosome and exhibit aggressive morphological changes under cooling treatment with spiny cactus-like shape to pierce endosome membrane, which brings about the hydrolytic enzyme inside the endosome, and packaged drugs released into the cytosol to kill cells (Figure 1). The Ga particles injected into tumor sites can play both energy conversion enhancer and morphological change transformer roles under freezing treatment, and therefore demonstrate remarkable cancer cell killing efficacy in *in vivo* antitumor therapy with Ga/MPs + cryo and Ga/M/PPs + cryo groups having higher survival rates in all groups. The

cryo-facilitated LM particle transformer-Ga/M/PPs have several advantages: (1) good tumor targeting: Ga/M/PPs based on cancer cell membrane have good tumor targeting for the homotypic binding. (2) Long-term retention in the tumor: the retention time of Ga/M/PPs was longer than 2 weeks, which was higher than that of GaPs. (3) Great cryotherapy effect: Ga/MPs + cryo and Ga/M/PPs + cryo groups displayed higher survival rate compared with that of GaPs + cryo. Therefore, such cryo-responsive materials with obvious shape transformation are promising for expanding active targeting tumor therapeutics, especially for intracellular therapy.

## RESULTS AND DISCUSSION

### Fabrication and characterization of Ga transformers

A schematic illustration of the preparation process to assemble Ga particles is shown in [Figure 2A](#). First, Ga particles were obtained by sonicating pure metal Ga for 20 min in chitosan oligosaccharide (COS) solution to ensure a particle size of approximately 1  $\mu\text{m}$  in diameter. Second, the fabricated Ga particles were coated with cell membrane, which was directly extracted from C8161 cells to assemble Ga particles, as well as loading drugs. The prepared particles appeared as core-shell structure with evenly coated cell membrane and displayed distinct shape transformation like cactus under freezing treatment. The particle sizes of GaPs, Ga/MPs, and Ga/M/PPs, which were all approximately 1  $\mu\text{m}$ , are shown in [Figure S1](#). The cell membrane outside GaPs on the large version of Ga/MP TEM images was clearly observed, because of the contrast difference of Ga particle and cell membrane ([Figure S2](#)).

To study the freezing-facilitated shape transformation, GaPs and Ga/MPs were exposed to liquid nitrogen for a short time, and the morphology of GaPs and Ga/MPs both at room temperature and freezing conditions were observed by TEM images. These GaPs and Ga/MPs exhibited similar external appearance as regular spheres at room temperature ([Figure 2B<sub>1</sub>](#) and [2C<sub>1</sub>](#)). However, GaPs and Ga/MPs showed entirely different shapes after being treated with liquid nitrogen freezing, as observed by cryo-TEM. For GaPs, many fragmented particles were generated and were scattered around during the freezing process, marked by the yellow arrows in [Figures 2B<sub>2</sub>](#) and [2B<sub>3</sub>](#). The process by which Ga fragments fell from the GaPs surface layer after freezing treatment was similar to the one by which animals sloughed. After rewarming, the scattered fragments still existed around GaPs and could not be restored to the original shape when the temperature rose ([Figure S3](#)). [Figure 2B<sub>4</sub>](#) shows the particle size distribution of GaPs measured by dynamic light scattering (DLS) before and after freezing treatment, indicating that GaP particle size decreased because of freezing treatment, which was consistent with the TEM images.

For Ga/MPs, after wrapping a layer of cell membrane around GaPs, the cell membrane could protect GaPs from breaking under freezing condition, and [Figure S4](#) shows the TEM image of C8161 cell membrane. Cryo-TEM clearly showed that severe deformation took place on Ga/MPs under freezing treatment and thus produced lots of spikes around the particle surface. The transformed Ga/MPs looked like cactus ([Figure 2A](#) shows the schematic diagram, and [Figure 2C<sub>2</sub>](#), [2C<sub>3</sub>](#), and [S5](#) show the corresponding cryo-TEM images). After rewarming to room temperature, Ga/MPs were restored to their original regular spheres ([Figure S6](#)). Meanwhile, their particle sizes did not have an obvious change before and after freezing ([Figure 2C<sub>4</sub>](#)). There were two possible reasons for the mechanism of the dramatic shape transformation of Ga/MPs under freezing. First, Ga demonstrated abnormal volume

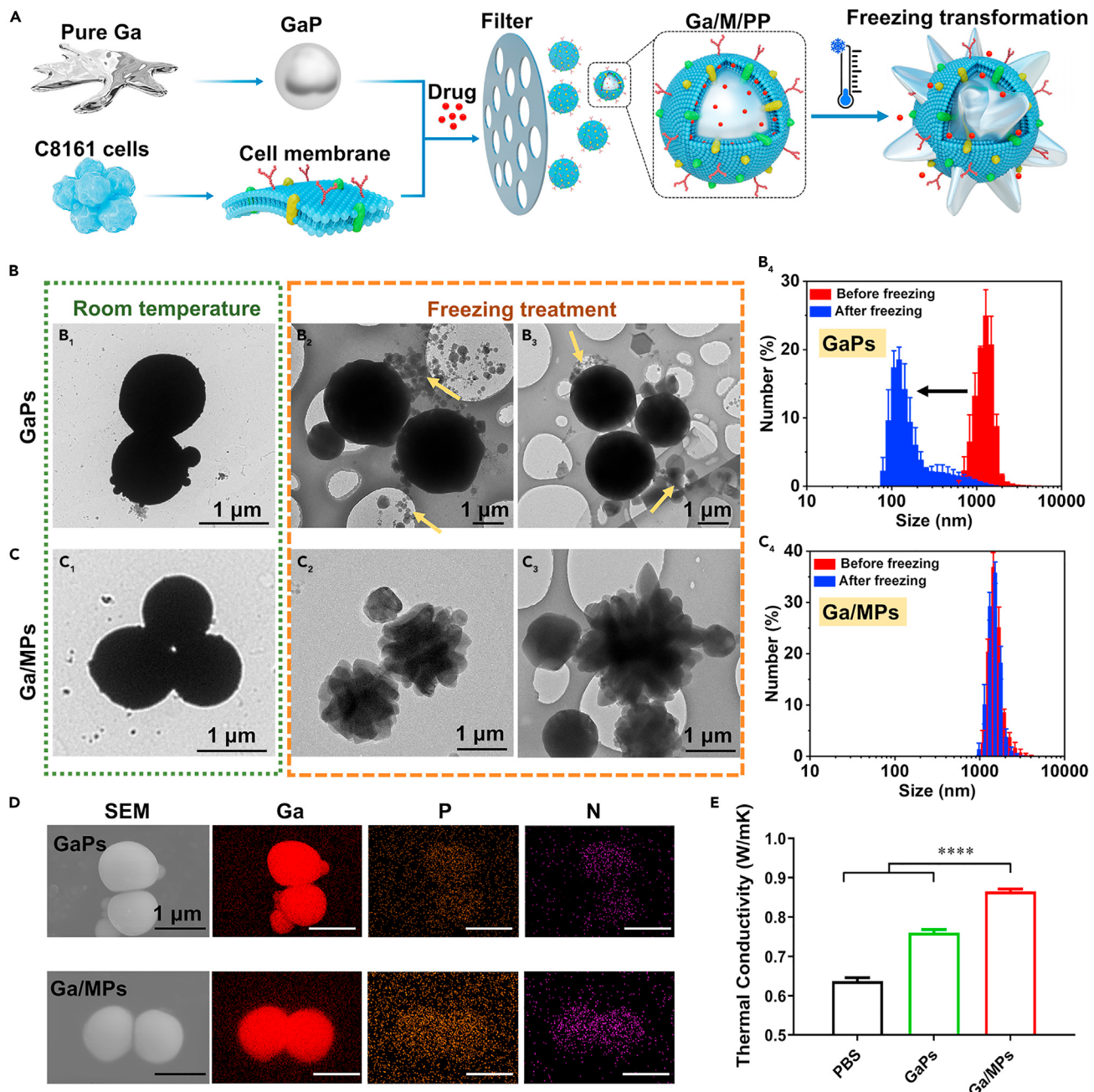


**Figure 2. Preparation and characterization of Ga particles materials**

(A) Preparation process of Ga/M/PP and its freezing transformation.

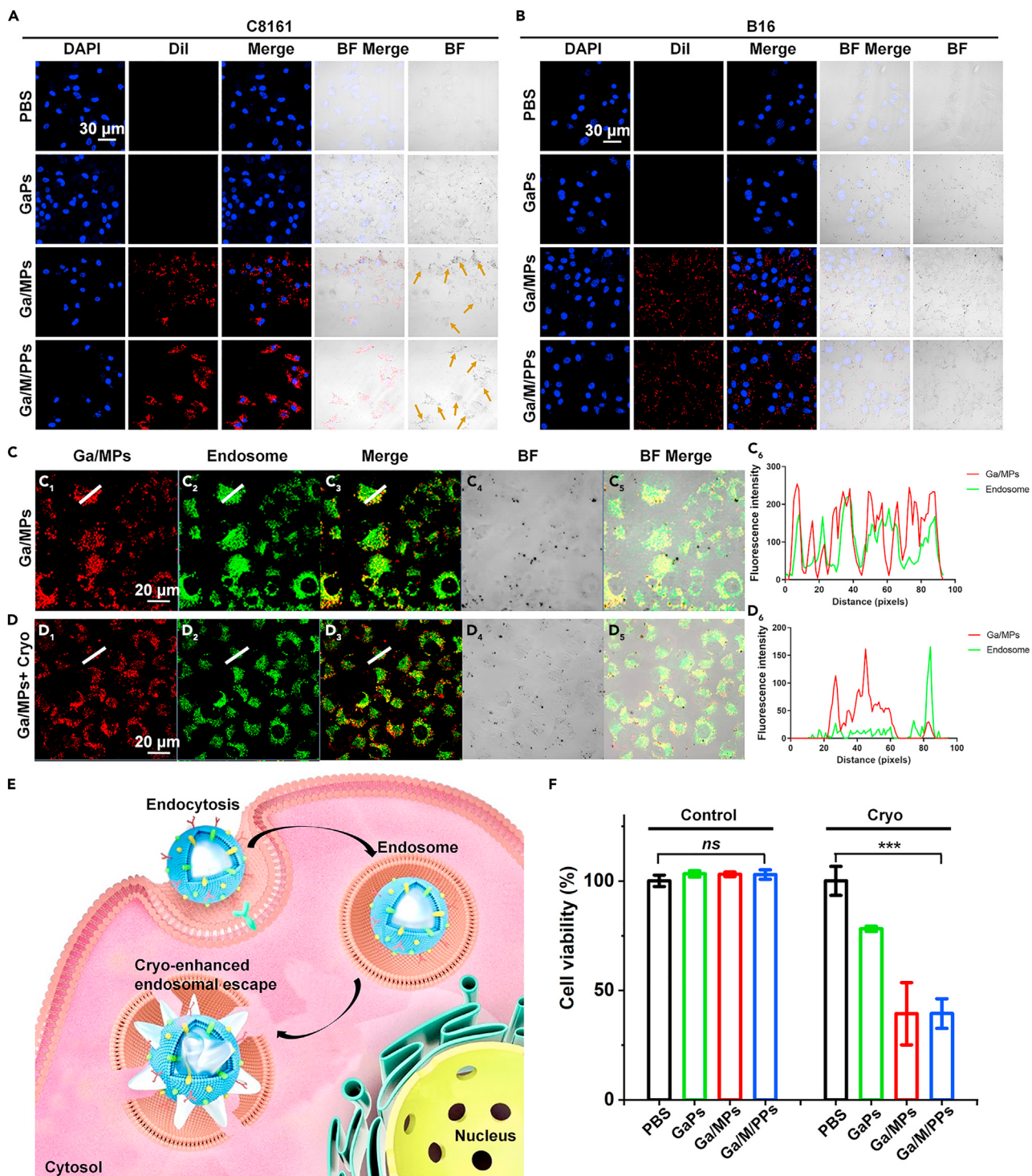
(B) TEM images of GaPs, (B<sub>1</sub>) TEM image of GaPs at room temperature, (B<sub>2</sub> and B<sub>3</sub>) cryo-TEM images of GaPs under freezing treatment at -196°C, Ga fragments marked by the yellow arrows, (B<sub>4</sub>) particle size (diameter, nm) of GaPs before and after freezing treatment by DLS.

(C) TEM images of Ga/MPs, (C<sub>1</sub>) TEM image of Ga/MPs at room temperature, (C<sub>2</sub> and C<sub>3</sub>) cryo-TEM images of Ga/MPs under freezing treatment at -196°C, (C<sub>4</sub>) particle size (diameter, nm) of Ga/MPs before and after freezing treatment by DLS.

(D) SEM images and EDS maps of GaPs and Ga/MPs.

(E) Thermal conductivity of PBS, GaPs, and Ga/MPs, respectively. The data show the mean  $\pm$  s.e.m. from a representative experiment ( $n = 3$ ), and analyzed by one-way ANOVA, \*\*\*\* represents  $p < 0.0001$ . All scale bars: 1  $\mu$ m.

expansion during phase transition; that is, Ga could expand its volume during phase transition from liquid to solid when temperature falls.<sup>50-52</sup> Second, freezing treatment could cause the cell membrane to rupture, the ruptured cell membrane served

**Figure 3. Endosomal escape of Ga particle transformation**(A) Cell uptake of GaPs, Ga/MPs, and Ga/M/PPs after co-incubation with C8161 cells for 4 h. Scale bar: 30  $\mu$ m.(B) Cell uptake of GaPs, Ga/MPs, and Ga/M/PPs after co-incubation with B16 cells for 4 h. Scale bar: 30  $\mu$ m.(C) Localization of Ga/MPs and endosomes in C8161 cells after incubation for 4 h: (C<sub>1</sub>) localization of Dil-Ga/MPs in C8161 cells; (C<sub>2</sub>) localization of endosomes in C8161 cells; (C<sub>3</sub>) merged image of (C<sub>1</sub>) and (C<sub>2</sub>); (C<sub>4</sub>) BF image; (C<sub>5</sub>) BF merged image of (C<sub>3</sub>) and (C<sub>4</sub>); (C<sub>6</sub>) co-localization of Ga/MPs and endosomes in C8161 cells calculated by ImageJ. Scale bar: 20  $\mu$ m.

**Figure 3. Continued**

(D) Localization of Ga/MPs and endosomes in C8161 cells after incubation for 4 h and cryo-treatment: (D<sub>1</sub>): localization of Dil-Ga/MPs in C8161 cells after cryo-treatment; (D<sub>2</sub>) localization of endosomes in C8161 cells after cryo-treatment; (D<sub>3</sub>) merged image of (D<sub>1</sub>) and (D<sub>2</sub>); (D<sub>4</sub>) BF image; (D<sub>5</sub>) BF merged image of (D<sub>3</sub>) and (D<sub>4</sub>); (D<sub>6</sub>) co-localization of Ga/MPs and endosomes in C8161 cells calculated by ImageJ. Scale bar: 20 μm.

(E) Schematic illustration of cryo-facilitated endosomal escape caused by Ga/MPs' mechanical destruction of endosome.

(F) *In vitro* cell cytotoxicity of three Ga particles (GaPs, Ga/MPs, Ga/M/PPs) in the control group (incubation at room temperature for 5 min) and cryo group (incubation at -80°C for 5 min). The data show the mean ± s.e.m. from a representative experiment (n = 3), and analyzed by one-way ANOVA, \*\*\* represents p < 0.001.

as the bonding point for solidification and crystallization of Ga, and therefore dendrites were formed outside the Ga/MPs, which presented as cactus-like structures.<sup>53–55</sup>

The element mapping data of GaPs and Ga/MPs obtained from an energy-dispersive spectrometer (EDS) demonstrated the existence of P and N in Ga/MPs, and the absence of P and N in GaPs (Figure 2D). The existence of P and N in Ga/MPs was mainly contributed by the C8161 cell membrane. Meanwhile, X-ray diffraction (XRD) measurement of GaPs in Figure S7A indicated the considerable presence of Ga<sub>2</sub>O<sub>3</sub> and Ga, and the result of Ga/MPs in Figure S7B indicated the considerable presence of Ga<sub>2</sub>O<sub>3</sub>, Ga, P, and C. Moreover, from the thermal conductivity measurement (Figure 2E), GaPs and Ga/MPs displayed better thermal conductivities in comparison with PBS solution, and thus better energy transfer due to the addition of Ga metal. Besides, we have also measured the surface zeta potential of GaPs and Ga/MPs, with the results of 57 mV on GaPs surface and -7 mV on Ga/MPs surface (Figure S8). Finally, the particle stability of GaPs and Ga/MPs has also been evaluated by measuring the particle sizes after a period of time, and the results showed that Ga/MPs were more stable than GaPs within 72 h (Figure S9). Ga/M/PPs showed good stability when incubated in PBS at room temperature, with no significant change observed in the mean size after 72 h (Figure S10).

#### Endosomal escape and cytotoxicity of Ga transformers

In order to validate the Ga/MPs' targeting capability of human melanoma cells, the cellular uptake of Ga/MPs by human melanoma cell C8161 and mouse melanoma cell B16 were evaluated. In the cell uptake experiment, 4',6-diamidino-2-phenylindole (DAPI) was applied to label the cell nucleus with blue fluorescence, and 1,1'-di-octadecyl-3,3,3',3'-tetramethylindocarbocyanine perchlorate (Dil) to mark the cell membrane outside Ga/MPs with red fluorescence. A picture captured by confocal laser scanning microscopy (CLSM) showed that a large amount of Ga/MPs and Ga/M/PPs were taken into C8161 cells after co-incubation for 4 h (Figure 3A). On the contrary, only a small amount of Ga/MPs and Ga/M/PPs were taken into B16 cells after co-incubation for 4 h (Figure 3B). Additionally, from the bright field (BF) images in Figures 3A and 3B, it can be seen that the Ga particles (seen as black spots) are uniformly distributed in GaPs-C8161, GaPs-B16, Ga/MPs-B16, and Ga/M/PPs-B16 groups. High-density distributions (yellow arrow) were only observed for Ga/MPs-C8161 and Ga/M/PPs-C8161 groups. Therefore, the Ga/MPs and Ga/M/PPs had prominent targeting capability of C8161 cells in comparison with B16 cells. Additionally, the approach of assembling particles with cell membrane from the same tumor cell origin provided a versatile strategy with low immunogenicity to diminish particles' immune response in *in vivo* therapy.

In order to evaluate the endosomal escape capability of Ga/MPs, the co-localization of Ga/MPs with endosomes in C8161 cells was done and then analyzed. Ga/MPs were labeled with Dil (red) and shown in Figures 3C<sub>1</sub> and 3D<sub>1</sub>. In addition, endosomes were stained with Lysotracker, as indicated by green spots in Figures 3C<sub>2</sub>

and 3D<sub>2</sub>. After incubation with C8161 cells for 4 h, a majority of Ga/MPs were observed inside the endosomes (Figure C<sub>3-6</sub>). Ga/MPs inside endosomes are indicated by the yellow dots (overlap of red and green dots) in Figures 3C<sub>3</sub> and 3D<sub>3</sub>. In contrast, the co-localization of Ga/MPs and endosomes significantly reduced after cryo-treatment, indicating that cryo-treatment could enable successful endosomal escape of Ga/MPs (Figures 3D<sub>4-6</sub>). Moreover, *in vitro* cytotoxicity experiments were performed in C8161, B16, and HaCaT cells. It was observed that GaPs, Ga/MPs, and Ga/M/PPs had no significant cytotoxicity on C8161 cells after co-culture with C8161, B16, and HaCaT cells for 24 h in the control group (Figures 3F and S11). Meanwhile, GaPs, Ga/MPs, and Ga/M/PPs had severe cytotoxicity on C8161, B16, and HaCaT cells after co-cultivation for 24 h in the cryo groups (Figures 3F and S12). The *in vitro* antitumor efficacy of Ga/MPs and Ga/M/PPs was better, contrasting with that of GaPs (Figure 3F), indicating that the cell membrane-coated Ga particles have tremendous potential for melanoma cryotherapy.

The cell membrane employed to encapsulate GaPs was extracted from human C8161 cells and the collected C8161 cell membrane retained incredible retention of main membrane proteins even after coating on particles. Hence, the assembled Ga/MPs had abundant specific membrane protein to target C8161 cells and, on the contrary, to fail identifying mice B16 cells from different origins, which illustrated the distinct homologous targeting capability with the same-origin tumor cells. The aforementioned results were also consistent with the reported research that the cell membrane outside particles could contribute to tumor targeting.<sup>56,57</sup> After being recognized by tumor cells, Ga/MPs entered the endosome by endocytosis. Without freezing exposure, the endosomal membrane maintained an undamaged state with no cell death in cell viability tests (control group in Figure 3F). After cryo-treatment, a noticeable morphological transformation had happened with endosomal membrane disruption by the remarkable Ga/MPs shape change. The result was consistent with the cell viability results of cryo groups (Figure 3F). Collectively, freezing-triggered shape transformation of Ga/MPs could physically pierce the endosomal membrane and contribute to endosomal escape (Figure 3E), and hence could be used to facilitate intracellular treatment.

#### ***In vivo* antitumor cryotherapy**

To realize *in vivo* tumor therapy with synchronized cryoablation and endosomal escape destructive mechanism, C8161-bearing nude mice were used for the anti-tumor efficacy evaluation. Then GaPs, Ga/MPs, and Ga/M/PPs were injected into tumor tissue 1 day ahead of cryo-treatment allowing adequate time (more than 20 h) to ensure all the tumor cells could absorb the particles. Black appearance of tumors showed immediately after successful injection of GaPs, Ga/MPs, and Ga/M/PPs into tumor tissue (Figure S13). PBS solution injected into mice tissue served as a blank control group to reveal the lethality of cryoablation alone. During cryotherapy, the cryoprobe was directly inserted into the center of the tumor and an ice ball embracing the tumor was formed (Figure S14). As shown in Figure 4A, thermal infrared images under the cryoprobe showed that the tumor tissue was obviously cooled by the cryoprobe apparatus within 4 min. The temperature of the cryoprobe was controlled from -196°C to 76°C by liquid nitrogen for the rapid freezing process and subsequently ethanol was applied for the rewarming procedure (Figure 4B).

Under cryoablation cold exposures, rapid dropping of mice body temperature was expected and we applied an electric blanket for mice to keep them warm during treatments. From the view of tumor volume variation curves in Figures 4C and S15, the groups (1-PBS, 3-GaPs, 5-Ga/MPs, 7-Ga/M/PPs) without cryo-treatment

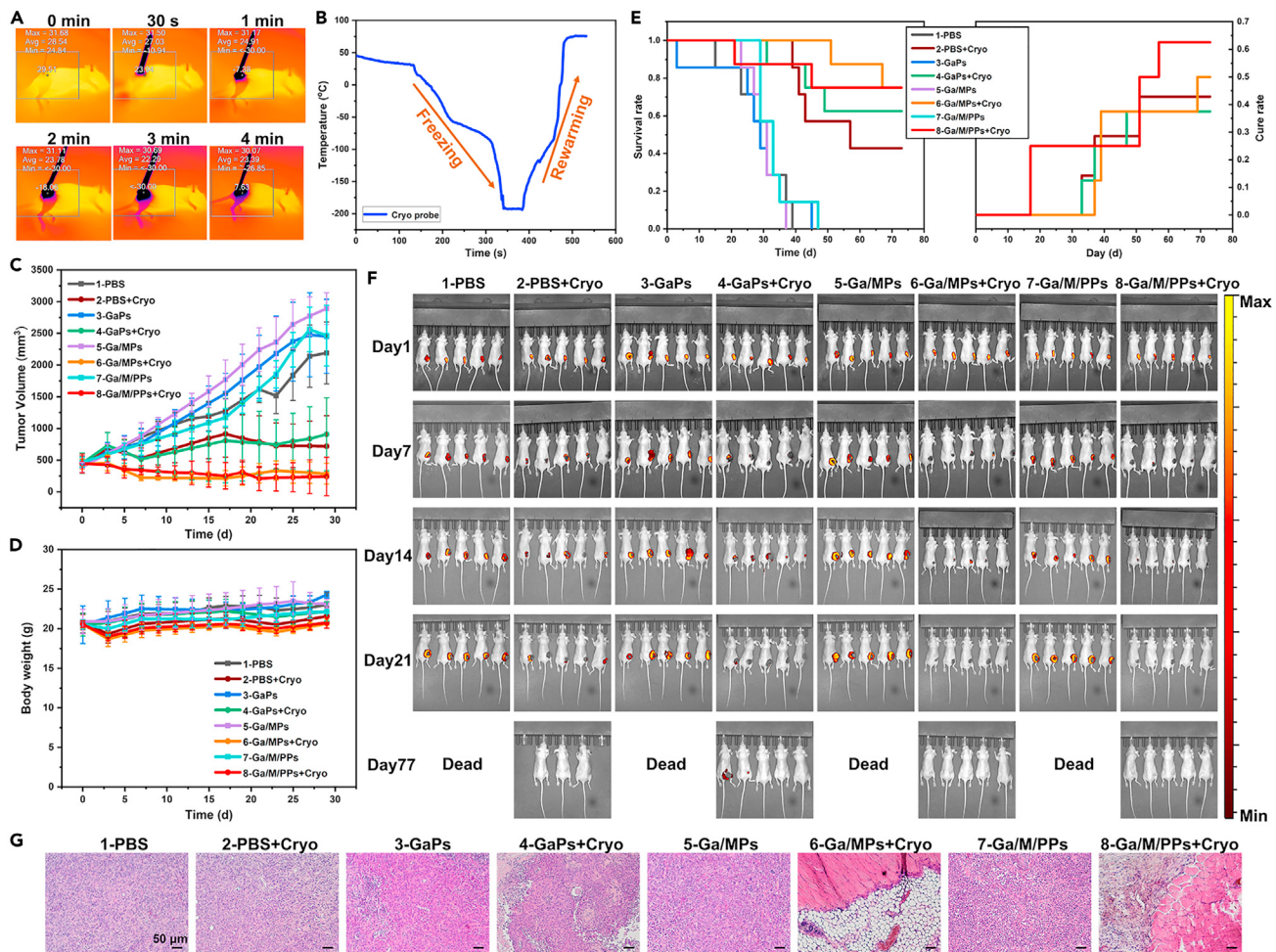


**Figure 4.** *In vivo* antitumor cryoablation with GaP materials

- (A) Thermal infrared images of tumor-bearing mice treated by cryoprobe.
- (B) Temperature variation of cryoprobe.
- (C) Tumor volume curves for the eight groups (1-PBS, 2-PBS + cryo, 3-GaPs, 4-GaPs + cryo, 5-Ga/MPs, 6-Ga/MPs + cryo, 7-Ga/M/PPs, 8-Ga/M/PPs + cryo).
- (D) Mice body weight curves.
- (E) Mice survival rate curves (left plots) and cure rate curves (right plots) of the eight groups with different treatments.
- (F) *In vivo* small animal optical images of the mice on the 1<sup>st</sup>, 7<sup>th</sup>, 14<sup>th</sup>, 21<sup>st</sup>, and 77<sup>th</sup> days.
- (G) H&E staining of tumor tissues for the eight groups after two treatments. Scale bars: 50 μm.

showed distinct tumor growth from ~400 mm<sup>3</sup> to ~3,000 mm<sup>3</sup> within 1 month. In the four cryo-treatment groups, we observed different tumor growth. On average, the tumor volume increased from ~400 mm<sup>3</sup> to ~800 mm<sup>3</sup> within 1 month in the 2-PBS + cryo group and 4-GaPs+cryo group, and thus showed a slowing in the rate of growth of tumor tissue. However, for the other two cryo groups (6-Ga/MPs + cryo and 8-Ga/M/PPs + cryo), antitumor treatments have prominently inhibited tumor growth, with the tumor volume decreased from ~400 mm<sup>3</sup> to ~200 mm<sup>3</sup>. Therefore, the above results presented totally opposite tumor growth trends of cryo-treatment groups in comparison with non-cryo groups. This was expected due to the tumor growth suppression of Ga/MP- and Ga/M/PP-treated groups with the assistance of an endosomal escape destruction mechanism. During the whole treatment, mice did not show unusual symptoms after cryosurgery and all vital signs appeared normal as their body weight remained stable (Figure 4D). As

a pre-eminent oncotherapy, cryotherapy had a great advantage for efficient pain relief with a frozen anesthesia function during the treatment process. This was in contrast to some well-explored tumor therapy methods, such as photothermal therapy (PTT), photodynamic therapy (PDT), magnetic hyperthermia (MH), and electrochemical therapy (EChT), which caused additional severe pain accompanied by weight loss and increased mortality.<sup>58–60</sup> The results mentioned above sufficiently proved that cryo-treatment could transform the Ga/MPs or Ga/M/PPs inside endosomes into shape deformation accompanied by strong mechanical force to destroy endosomal membrane and thus trigger endosomal escape mechanism to kill tumor cells.

To further evaluate antitumor efficacy of Ga/MPs or Ga/M/PPs and cryo-treatment, survival rate data of C8161-bearing nude mice were collected. The results showed that cryo-treatment improved mice life span in four cryo groups (2-PBS + cryo, 4-GaPs + cryo, 6-Ga/MPs + cryo, 8-Ga/M/PPs + cryo) in comparison with non-cryo groups (1-PBS, 3-GaPs, 5-Ga/MPs, 7-Ga/M/PPs). Herein, when the measured tumor volume of a mouse was less than 20 mm<sup>3</sup>, the mouse was considered as cancer free. The right plots of Figure 4E reflect the cure rate in the whole procedure. After 77 days of the experiment, we observed that three out of seven mice in the 2-PBS + cryo group were cured, three out of eight mice in the 4-GaPs + cryo group were cured, four out of eight mice in the 6-Ga/MPs + cryo group were cured, and five out of eight mice in the 8-Ga/M/PPs + cryo group were cured. Thus, the 8-Ga/M/PPs + cryo group with both Ga particles and drugs plus cryosurgery exhibited the best performance in the antitumor survival test with minimum recurrence. Therefore, it was concluded that a greater cancer cell death efficacy was observed in the 8-Ga/M/PPs + cryo group. Additionally, the *in vivo* tumor fluorescence images presented in Figure 4F show that the tumors in the cryo groups were ablated efficiently with distinct black scars left (Figure S16) after two cryo-treatments, which also coincided with the results of tumor growth volume in Figure 4C. Finally, plenty of tumor cells were observed in the hematoxylin-eosin (H&E) staining slices of four non-cryo groups (1-PBS, 3-GaPs, 5-Ga/MPs, 7-Ga/M/PPs) and two cryo groups (2-PBS + cryo, 4-GaPs + cryo), but none were discovered in the slices of 6-Ga/MPs + cryo and 8-Ga/M/PPs + cryo groups (Figure 4G). As well, the major mice organ slices revealed no visible abnormalities in each group, indicating that there was no tumor metastasis in lungs, livers, spleens, kidneys, and hearts (Figure S17). Overall, the combination of Ga/MPs and Ga/M/PPs with cryotherapy enabled *in vivo* mice cancer ablation with desirable efficacy as well as fast cancer elimination.

### High-resolution computed tomography imaging

Because of the high density of metal Ga (6.08 kg/m<sup>3</sup>),<sup>61</sup> Ga particles were radiopaque to some extent for simultaneously serving as contrast agents under X rays. On account of the small particle size (about 1 μm), high-resolution X-ray imaging could be carried out by GaPs. As shown in Figures 5A and S18, GaPs were injected from the renal vein to fill the kidney with clearly visible terminal vessels in X-ray images (right of Figure 5A). The computed tomography (CT) 3D structure reconstructed by micro-CT software distinctly reflected the distribution of blood vessels in kidney and liver (Figure 5B). The diameters of kidney terminal blood vessels after GaPs angiography were around 100–150 μm, and the diameters of liver terminal blood vessels were around 200–400 μm, both of which represented the injectability and radiopacity of GaPs solution. Furthermore, *in vivo* tumor-bearing mice CT scans were taken to demonstrate the antitumor efficiency. CT images of the PBS group showed nothing at the tumor site; however in the GaPs group a few spots of GaPs agents at the tumor site were observed 20 h after the injection (Figures 5C; Video S1). However, completely different CT imaging results were

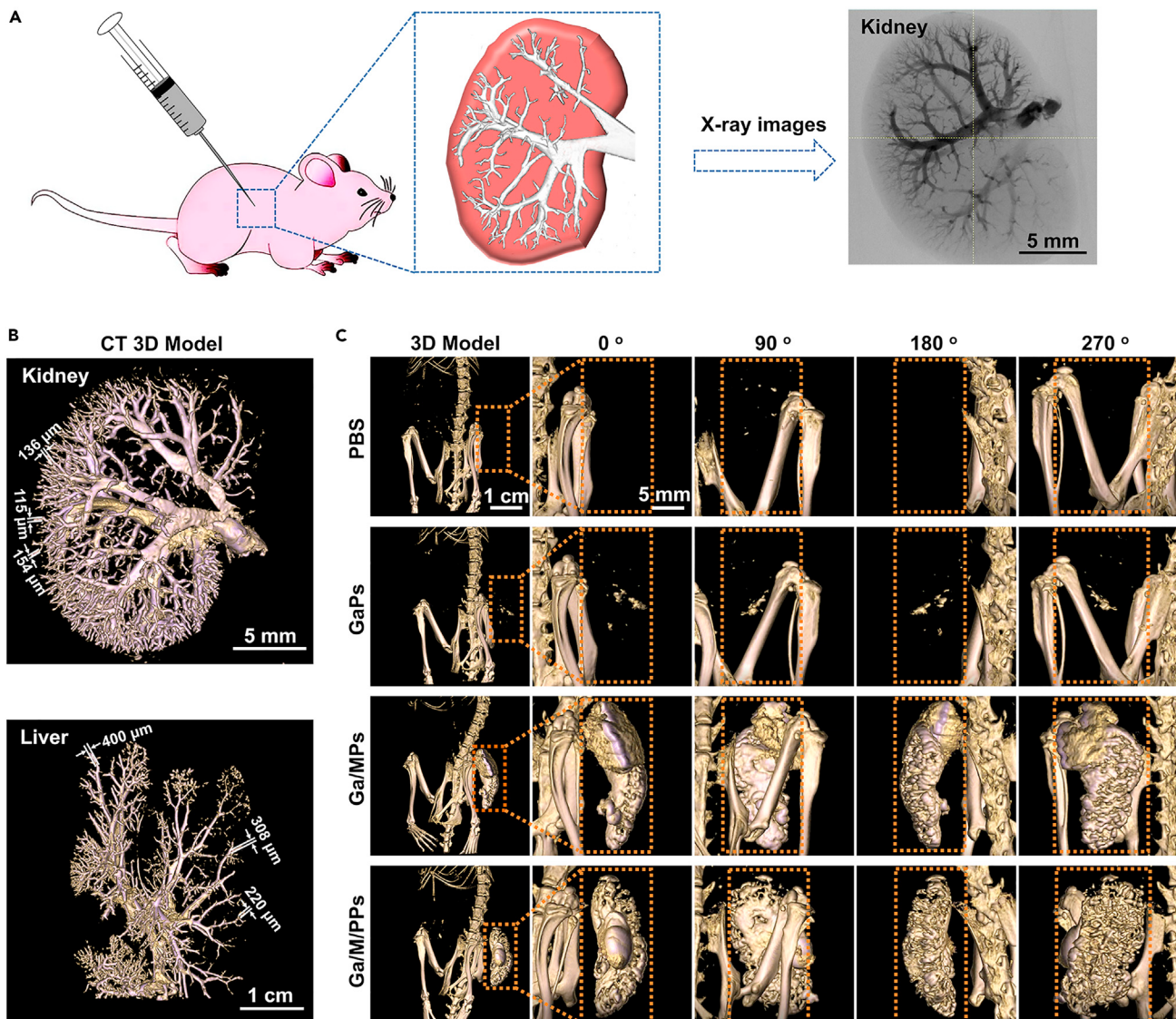


**Figure 5. High-resolution imaging under X-ray of Ga particles in *in vitro* organs and *in vivo* tumors**

(A) Illustrated scheme of the injection process of Ga particles solution into animal body and X-ray images of the kidney.

(B) Reconstructed micro-CT 3D models of rat kidney and liver organs with GaPs perfused into blood vessels, corresponding to the X-ray images in Figure 4A.

(C) Reconstructed micro-CT 3D models of tumor-bearing mice with four different solutions (PBS, GaPs, Ga/MPs, Ga/M/PPs) injected into tumor tissue under 0°, 90°, 180°, and 270°. Scale bars in 3D model column: 1 cm. Scale bars in 0°, 90°, 180°, and 270° columns: 5 mm.

observed with Ga/MPs and Ga/M/PPs groups under micro-CT with an obvious enhancement of tumor site imaging attributed to the targetability of cell membrane-coated outside particles (Figure 5C). In particular, the rebuilt 3D models of the tumors accurately reverted the tumor size and location, which provided plenty of reference information to doctors and hence intricate planning of subsequent therapy could be further improved. Besides, because of the radiopacity, the metabolism of Ga particles in the body could be observed by X ray. Therefore, CT imaging technology integrated with Ga particles could not only preserve the essence of CT imaging but also provide precise signals from blood vessels and tumors with Ga particles exhibiting excellent injectability, radiopacity, and targetability to enrich CT imaging information.

Researchers have done lots of investigation on the safe dosage of LM in living bodies for non-toxicity and identified its maximum tolerated dose (MTD) to be 700 mg/kg.<sup>1</sup> In our work, the Ga dosage in mouse body is 500 mg/kg and meets the requirement of MTD, which is no harm for the body. During CT imaging, we need to be very careful to control the dosage of GaP injected into the mouse body to avoid blood blockage, and also Ga has the ability to cause rapid metabolism.<sup>1,31</sup> To guarantee the safety of GaP in CT imaging without blood blockage risk, in our future work we need to enhance its imaging efficiency under CT with less GaP injected into the body and apply nano-sized GaP as X-ray contrast agent. We have designed experiments to evaluate the *in vivo* image of Ga/MPs and Ga/M/PPs. Ga/MPs and Ga/M/PPs in [Figure S19](#) exhibited excellent accumulation properties at the tumor site, showing remarkable tumor targetability of the cell membrane-evaporated particles. The fluorescence intensity enhanced rapidly in the first 8 h and then decreased slowly. Meanwhile, the Ga concentration in mice blood in [Figure S20](#) showed that, after the injection of particles for 72 h, Ga concentration reached a peak and then kept steady until 336 h, and finally all the Ga was almost metabolized after 672 h, which illustrated that Ga had strong metabolic capacity within 1 month.

### Conclusions

In summary, a series of freezing-driven LM transformable particles were developed to enhance endosomal escape with a physical mechanical destruction mechanism for targeted cell killing in intracellular tumor cryotherapy. Cell membrane-encapsulated Ga/MPs exhibited dramatic morphological deformation under cryo exposure along with cactus-like structure observed by cryo-TEM, while totally opposite morphology was displayed for GaPs accompanied by many fragmented particles generated outside the particles under freezing treatment. The cryo-triggered remarkable shape transformation of Ga/MPs with obvious volume increase contributed to the physical mechanical disruption of the endosomal membrane, and thus facilitated the endosomal escape and achieved the drug release inside Ga/M/PPs. Furthermore, *in vivo* results with distinct tumor growth suppression and cure rate improvement illustrated the significant tumor cryoablation efficiency with synergistic antitumor treatment of Ga particles and antitumor drugs plus cryo-treatment. Besides, the obtained GaPs exhibited prominent radiopacity to the terminal blood vessels under X rays to realize high-resolution *in vivo* imaging by directly injecting materials, and also the cell membrane-coated particles visualized the tumor size and location accurately due to the excellent targetability. Overall, the obtained LM transformers held great potential for developing enhanced endosomal escape with physical mechanical destruction to endosomal membrane in intracellular therapy, and therefore could generalize effective cell-lever cryosurgery.

In our future research, we plan to apply different tumor cell membranes for not only melanoma but also other kinds of tumors as a kind of versatile strategy in intracellular tumor therapy following up the highly efficient Ga particles transformers intracellular therapy, such as breast cancer, lung cancer, leukemia, and osteocarcinoma. Meanwhile, the LM-triggered tumor therapy can be combined with immunotherapy for more efficient cancer killing with the physical mechanical destruction capacity to realize the dual-mode therapy.

## EXPERIMENTAL PROCEDURES

### Resource availability

#### Lead contact

Jing Liu, e-mail ([jliubme@mail.tsinghua.edu.cn](mailto:jliubme@mail.tsinghua.edu.cn)).

**Materials availability**

This study did not generate new unique materials.

**Data and code availability**

The data presented in this work are available from the lead contact upon reasonable request.

**Preparation of GaPs, Ga/MPs, and Ga/M/PPs**

Metal Ga with the purity of 99.99% was applied for the preparation of a series of different Ga particles. Two grams of COS was dissolved in 50 mL of H<sub>2</sub>O to get a 40 mg/mL COS solution. Then 4 g of pure Ga metal was added into 40 mg/mL COS (10 mL). A sonication method (power, 200 W; T<sub>on</sub> = 4 s, T<sub>off</sub> = 4 s, 150 round) was utilized to produce GaPs. After that, 160 mg of GaPs were mixed with 1.6 mg of C8161 cell membrane (for the preparation method, refer to the section, “purification of cell membrane”) and sonicated in the ultrasonic bath at a frequency of 45 kHz and 400 W for thoroughly mixing. The mixture was extruding through a 5-μm polycarbonate membrane with an Avanti mini extruder to obtain the membrane-coated GaPs (Ga/MPs). Lastly, the membrane-coated GaP/paclitaxel (Ga/M/PPs) was prepared as follows: 160 mg of GaPs were mixed with 1.6 mg of C8161 cell membrane and 1.6 mg of PTX, then sonicated in the ultrasonic bath at a frequency of 45 kHz and 400 W for thoroughly mixing. After that, the mixture was extruded through 5-μm polycarbonate membrane with an Avanti mini extruder to obtain the drug-loaded and membrane-coated particles (Ga/M/PPs).

**Characterization of GaPs, Ga/MPs, and Ga/M/PPs**

To characterize the morphology of GaPs and Ga/MPs, 5 μL of GaP and Ga/MP solution were separately dropped onto carbon-coated copper grids and incubated for 1 min. The residual sample was removed by clean filter paper. After that, the samples were washed with double-distilled H<sub>2</sub>O (ddH<sub>2</sub>O) twice to remove the COS on GaP and Ga/MP samples. Then, Ga/MPs were negatively stained with 2% uranyl acetate for 2 min. Finally, the copper grids were dried at room temperature for 2 min and detected by TEM (HT7700, Japan).

The particle morphology images were captured with cryo-TEM (FEI Tecnai F20 TEM, Netherlands) to characterize the shape change at -196°C. Scanning electron microscopy (SEM; SU-8010, Japan) was applied to observe the particles' surface microstructure, as well as EDS for the investigation of element distribution of particles. XRD (SmartLab, Japan) measurements were applied to analyze the surface chemical composition of GaPs and Ga/MPs. The DLS method was utilized to measure the particle size using a Malvern Zetasizer (Nano ZSP 3600, UK) before and after freezing treatment. Meanwhile, the stability of GaPs, Ga/MPs, and Ga/M/PPs was evaluated by DLS when incubated in PBS solution at room temperature over 72 h. The thermal conductivity of the three solutions (PBS, GaPs, and Ga/MPs) was measured by thermal constants analyzer (Hot Disk TPS 2500S, Sweden).

**Cell culture**

C8161 human melanoma cells were kindly provided by Prof. Weiping Gao (Peking University, China). Wild-type B16-F10 mouse melanoma cells were purchased from ATTC. Human normal epidermal cells (HaCaT) were purchased from China National Biomedical Cell Resource. C8161/B16/HaCaT cells were maintained in DMEM complete medium containing DMEM basic medium (Multicell, United States), 10% fetal bovine serum (Gibco, United States), and 1% penicillin-streptomycin (Gibco, United States).

### Purification of cell membrane

The cell membrane from C8161 cells was purified according to previously published protocols.<sup>62</sup> Briefly, C8161 cells were suspended in the lysis buffer containing 0.25 M sucrose, 1 mM EDTA, 20 mM HEPES, and a cocktail of protease inhibitors (Sigma-Aldrich). After that, C8161 cells were sonicated using Ultrasonic Cell Disruption Apparatus (JY92-IIIN, China) for 30 rounds on ice (power, 200 W;  $T_{on} = 3$  s,  $T_{off} = 7$  s). Then the mixture was centrifuged at  $10,000 \times g$  for 25 min to remove the cell debris. Later on, the supernatant was centrifuged at  $150,000 \times g$  for 35 min to obtain a membrane pellet using a Beckman Coulter OPTIMA XPN-100 ultracentrifuge. Finally, the C8161 membrane pellet was suspended in PBS and stored at  $-80^{\circ}\text{C}$  for subsequent use.

### Cell uptake

First, the C8161/B16 cells in the logarithmic growth phase were seeded into confocal eight-well dishes ( $1.0 \times 10^4$  cells/dish) with DMEM complete medium. Then the cells were cultured at  $37^{\circ}\text{C}$  overnight to make them tightly adhere to the bottom of confocal eight-well dishes. Meanwhile, Ga/MPs and Ga/M/PPs were labeled with the red fluorescent dye Dil (10  $\mu\text{M}$ ) for 5 min, and the free Dil was removed by centrifugation and washed in PBS once. Then, GaPs, Dil-labeled Ga/MPs, and Ga/M/PPs were added into confocal eight-well dishes and incubated with C8161/B16 cells at  $37^{\circ}\text{C}$  for 4 h. Cells were washed in 200  $\mu\text{L}$  of PBS three times, and then fixed with 4% paraformaldehyde. After that, the cells were stained with 200  $\mu\text{L}$  of DAPI solution (1 ng/ $\mu\text{L}$ ) for 10 min at room temperature. Finally, the cell uptake of GaPs, Ga/MPs, and Ga/M/PPs by C8161/B16 cells was observed on a CLSM (Zeiss, Japan).

### Temperature-dependent deformation and endosomal escape

Before using the Ga/MPs *in vitro* and *in vivo*, the temperature-dependent transformation and the ability to achieve endosomal escape were evaluated. C8161 cells were incubated with Dil-labeled Ga/MPs for 4 h. Then C8161 cells (Ga/MPs + cryo group) were placed at  $-80^{\circ}\text{C}$  for 5 min. Meanwhile, C8161 cells (negative control, Ga/MPs group) were placed at room temperature for 5 min. The cells were then washed with PBS and stained with Lysotracker Deep Red (endosomal staining) for 20 min. After that, the co-localizations of Ga/MPs and endosomes were observed under laser confocal scanning microscope (with ZEN 2010 software).

### In vitro cytotoxicity

C8161/B16/HaCaT cells in the logarithmic growth phase were digested and seeded in a 96-well plate with DMEM complete medium at a density of 4,000 cells per well. All the cells were cultured at  $37^{\circ}\text{C}$  overnight to make them tightly adhere to the confocal dish. After that, 100  $\mu\text{L}$  of PBS, GaPs, Ga/MPs, and Ga/M/PPs mixture were added into 10 mL of DMEM complete medium. Subsequently, PBS, GaPs (400 ng/ $\mu\text{L}$ ), Ga/MPs (400 ng/ $\mu\text{L}$ ), and Ga/M/PPs (400 ng/ $\mu\text{L}$ ) in DMEM complete medium were co-cultured with cells for 24 h. Later on, *in vitro* cell cytotoxicity was evaluated by culturing the cells at room temperature (control group), or  $-80^{\circ}\text{C}$  for 5 min (cryo group). Then, the cells were washed in PBS three times to remove free materials. Finally, CCK-8 assay (Solarbio, China) was applied to detect the cell viability. The data show the mean  $\pm$  SEM from a representative experiment ( $n = 3$ ), and were analyzed by one-way ANOVA(\* $p < 0.05$ , \*\* $p < 0.01$ , \*\*\* $p < 0.001$ , \*\*\*\* $p < 0.0001$ ).

### Animal models

All BALB/c nude mouse (8 weeks old, female, average weight 20 g) were purchased from Vital River Laboratories (China) and fed at Tsinghua University, and  $2 \times 10^6$  C8161 cells in logarithmic growth phase were collected and subcutaneously injected

into the back of a BALB/c nude mouse. *In vivo* cryotherapy conducted when the tumor grew to around 400 mm<sup>3</sup>. We used the formula  $V = ab^2/2$  to calculate tumor volume ( $a$  is the length of tumor,  $b$  is the width of tumor).

#### ***In vivo* tumor cryotherapy**

C8161-bearing mice were randomly divided into eight groups: 1-PBS group (only 100 μL of PBS injected into tumor tissue,  $n = 7$ ), 2-PBS + cryo group (100 μL of PBS injected into tumor tissue and treated with cryoablation on tumor site,  $n = 7$ ), 3-GaPs group (only 100 μL of GaPs solution injected into tumor tissue,  $n = 7$ ), 4-GaPs + cryo group (100 μL of GaPs solution injected into tumor tissue and treated with cryoablation on tumor site,  $n = 8$ ), 5-Ga/MPs group (only 100 μL of Ga/MPs solution injected into tumor tissue,  $n = 7$ ), 6-Ga/MPs group (100 μL of Ga/MPs solution injected into tumor tissue and treated with cryoablation on tumor site,  $n = 8$ ), 7-Ga/M/PPs group (only 100 μL of Ga/MPs solution injected into tumor tissue and treated with cryoablation on tumor site,  $n = 7$ ), and 8-Ga/M/PPs group (100 μL of Ga/MPs solution injected into tumor tissue and treated with cryoablation on tumor site,  $n = 8$ ). The dose of Ga was 500 mg/kg in the groups 3-GaPs, 4-GaPs + cryo, 5-Ga/MPs, 6-Ga/MPs, 7-Ga/M/PPs, and 8-Ga/M/PPs. The cryoablation treatment was implemented by the cryoablation system (HYG-II, Beijing, China) with the cryoprobe directly inserted into tumor *in situ* (cryoprobe size: diameter, 1.7 mm).

The particle solutions were injected 1 day before cryoablation so that they could be fully absorbed into the endosomes of tumor cells before cryotherapy. Tumor-bearing mice were inserted into the cryoprobe for 4 min and were treated once every 7 days, and the cryoablation was repeated twice in total. The temperatures of mice body and cryoprobe were monitored by infrared camera (FLUKE Ti400, United States) and thermocouple, respectively. The data for mice body weight and tumor size were recorded every 2 days, at the same time, and the tumor growth was observed by *in vivo* small animal optimal imaging device (IVIS Spectrum, PerkinElmer, United States). When tumors grew to over 3,000 mm<sup>3</sup>, mice were euthanized. After 30 days, the tumor tissues as well as major organs (lung, liver, spleen, kidney, and heart) were resected for histological analysis through H&E staining. All animal protocols in the experiments were approved by the Institutional Animal Care and Use Committee (IACUC) of Tsinghua University, Beijing, China, under contract no. SYXK(Jing)2014-0024.

#### ***In vivo* image and metabolism**

First, Ga/MPs and Ga/M/PPs were stained by 10 μM 1,1'-dioctadecyl-3,3,3',3'-tetramethylindotricarbocyanine iodide (DiR) for 30 min to get DiR-labeled Ga/MPs and Ga/M/PPs (DiR-Ga/MPs, DiR-Ga/M/PPs). Then 10 mg of DiR-Ga/MPs and DiR-Ga/M/PPs were injected into C8161-bearing mouse by intratumoral injection when the tumor grew to around 100 mm<sup>3</sup>. Finally, fluorescent images of C8161-bearing mice ( $n = 3$ ) after intravenous injection of Ga/MPs and Ga/M/PPs for different time points (1 h, 4 h, 8 h, 24 h, 72 h, and 120 h) were obtained using an *in vivo* fluorescence imaging system (IVIS Spectrum, PerkinElmer, United States). Meanwhile, we also measured the concentration of Ga of mice blood from caudal vein of tumor-bearing mice after injecting 500 mg/kg at the tumor site. The Ga concentration in mice blood was measured by inductively coupled plasma mass spectrometry (ICP-MS; Thermo XSeries II ICP-MS, Thermo Fisher Scientific, Germany) after the injection of GaPs, Ga/MPs, and Ga/M/PPs at different time points (1 h, 4 h, 10 h, 24 h, 72 h, 120 h, 168 h, 336 h, 504 h, and 672 h).

#### **Micro-CT and X-ray imaging**

Ga particles as a contrast agent was employed for high-resolution imaging in blood vessels and tumors. After general anesthesia of Sprague Dawley (SD) rats, GaPs

solution was injected respectively from renal vein and hepatic portal vein to implement the GaPs contrast agent perfusion of blood vessels into kidney and liver. After completing the perfusion, small animal micro-CT apparatus (Quantum GX micro-CT, PerkinElmer, United States) with 90-kV voltages was applied to scan the kidney and liver. High-resolution 3D CT models were constructed by micro-CT software to observe the vascular distribution of kidney and liver organs. Furthermore, tumor-bearing mice were scanned by micro-CT after the injection of four kinds of different solutions (PBS, GaPs, Ga/MPs, Ga/M/PPs) for 20 h. The rebuilt micro-CT 3D models of tumor tissues were clearly presented for cell membrane-coated particles (Ga/MPs, Ga/M/PPs) in contrast to control PBS solution and bare GaPs.

## SUPPLEMENTAL INFORMATION

Supplemental information can be found online at <https://doi.org/10.1016/j.matt.2021.11.006>.

## ACKNOWLEDGMENTS

This work was supported by the National Natural Science Foundation of China under grant no. 51890893 and no. 91748206, the National Key Research and Development Program of China under grant no. 2020YFC0122301 and no. 2020YFC0122302, and the Fundamental Research Funds for the Central Universities no. KG16052901 and no. KG16115601.

## AUTHOR CONTRIBUTIONS

X.W. and J.C. conceived the research project. J.L. and J.C. supervised the research project, and participated in data analysis and/or manuscript revising. X.W. and J.C. conducted most of the experiments and writing of the paper. X.L. provided the HYG-II cryoablation system and helped *in vivo* tumor cryosurgery. S.S. helped to fabricate Ga particles. M.D., X.Z., and Y.C. assisted to finish the CT imaging experiments. G.Q. assisted to accomplish the manuscript revision. H.W., X.S., L.S., W.R., and L.H. provided many suggestions on the experimental design, data analysis, and manuscript revision.

## DECLARATION OF INTERESTS

The authors declare no competing interests.

Received: June 24, 2021

Revised: September 10, 2021

Accepted: November 2, 2021

Published: November 29, 2021

## REFERENCES

1. Yan, J., Lu, Y., Chen, G., Yang, M., and Gu, Z. (2018). Advances in liquid metals for biomedical applications. *Chem. Soc. Rev.* 47, 25182533.
2. Wang, Q., Yu, Y., and Liu, J. (2017). Preparations, characteristics and applications of the functional liquid metal materials. *Adv. Eng. Mater.* 20, 1700781.
3. Yang, J., Cheng, W., and Kalantar-Zadeh, K. (2019). Electronic skins based on liquid metals. *Proc. IEEE* 107, 2168–2184.
4. Wang, X., and Liu, J. (2016). Recent advancements in liquid metal flexible printed electronics: properties, technologies, and applications. *Micromachines* 7, 206–223.
5. Chu, K., Song, B., Yang, H., Kim, D., Lee, C., Park, M., and Chung, C. (2018). Smart passivation materials with a liquid metal microcapsule as self-healing conductors for sustainable and flexible perovskite solar cells. *Adv. Funct. Mater.* 28, 1800110.
6. Jeong, Y., Kim, J., Xie, Z., Xue, Y., Won, S., Lee, G., Jin, S., Hong, S., Feng, X., Huang, Y., et al. (2017). A skin-attachable, stretchable integrated system based on liquid GaInSn for wireless human motion monitoring with multi-site sensing capabilities. *NPG Asia Mater.* 9, e443.
7. Gao, Y., Ota, H., Schaler, E., Chen, K., Zhao, A., Gao, W., Fahad, H., Leng, Y., Zheng, A., Xiong, F., et al. (2017). Wearable microfluidic diaphragm pressure sensor for health and tactile touch monitoring. *Adv. Mater.* 29, 1701985.
8. Wang, X., Zhang, Y., Guo, R., Wang, H., Yuan, B., and Liu, J. (2018). Conformable liquid metal printed epidermal electronics for smart physiological monitoring and simulation treatment. *J. Micromech. Microeng.* 28, 034003.
9. He, Y., Zhao, Y., Fan, L., Wang, X., Duan, M., Wang, H., Zhu, X., and Liu, J. (2021). Injectable

- affinity and remote magnetothermal effects of Bi-based alloy for long-term bone defect repair and analgesia. *Adv. Sci.* 2100719.
10. Fan, L., Duan, M., Xie, Z., Pan, K., Wang, X., Sun, X., Wang, Q., Rao, W., and Liu, J. (2019). Injectible and radiopaque liquid metal/calcium alginate hydrogels for endovascular embolization and tumor embolotherapy. *Small* 16, 1903421.
  11. Wang, Q., Yu, Y., Pan, K., and Liu, J. (2014). Liquid metal angiography for mega contrast X-ray visualization of vascular network in reconstructing *in vitro* organ anatomy. *IEEE Trans. Biomed. Eng.* 61, 2161–2166.
  12. Wang, X., Fan, L., Zhang, J., Sun, X., Chang, H., Yuan, B., Guo, R., Duan, M., and Liu, J. (2019). Printed conformable liquid metal e-skin-enabled spatiotemporally controlled bioelectromagnetics for wireless multisite tumor therapy. *Adv. Funct. Mater.* 29, 1907063.
  13. Wang, X., Yao, W., Guo, R., Yang, X., Tang, J., Zhang, J., Gao, W., Timchenko, V., and Liu, J. (2018). Soft and moldable Mg-doped liquid metal for conformable skin tumor photothermal therapy. *Adv. Healthc. Mater.* 7, 1800318.
  14. Sun, X., Yuan, B., Rao, W., and Liu, J. (2017). Amorphous liquid metal electrodes enabled conformable electrochemical therapy of tumors. *Biomaterials* 146, 156–167.
  15. Wang, X., Guo, R., and Liu, J. (2018). Liquid metal based soft robotics: materials, designs, and applications. *Adv. Mater. Technol.* 4, 1800549.
  16. Sun, X., Yuan, B., Wang, H., Fan, L., Duan, M., Wang, X., Guo, R., and Liu, J. (2021). Nanobiomedicine based on liquid metal particles and allied materials. *Adv. Nanobiomed. Res.* 1, 2000086.
  17. Wang, H., Yao, Y., Wang, X., Sheng, L., Yang, X., Cui, Y., Zhang, P., Rao, W., Guo, R., Liang, S., et al. (2019). Large-magnitude transformable liquid-metal composites. *ACS Omega* 4, 2311–2319.
  18. Sheng, L., Zhang, J., and Liu, J. (2014). Diverse transformations of liquid metals between different morphologies. *Adv. Mater.* 26, 6036–6042.
  19. Cao, L., Yu, D., Xia, Z., Wan, H., Liu, C., Yin, T., and He, Z. (2020). Ferromagnetic liquid metal putty-like material with transformed shape and reconfigurable polarity. *Adv. Mater.* 32, 2000827.
  20. Ford, M., Ambulo, C., Kent, T., Markwick, E., Pan, C., Malen, J., Ware, T., and Majidi, C. (2019). A multifunctional shape-morphing elastomer with liquid metal inclusions. *Proc. Natl. Acad. Sci. U S A* 116, 21438–21444.
  21. Zhang, J., Sheng, L., and Liu, J. (2014). Synthetically chemical-electrical mechanism for controlling large scale reversible deformation of liquid metal objects. *Sci. Rep.* 4, 7116.
  22. Wang, H., Chen, S., Li, H., Chen, X., Cheng, J., Shao, Y., Zhang, C., Zhang, J., Fan, L., Chang, H., et al. (2021). A liquid gripper based on phase transitional metallic ferrofluid. *Adv. Funct. Mater.* 30, 2100274.
  23. Chen, S., Yang, X., Cui, Y., and Liu, J. (2018). Self-growing and serpentine locomotion of liquid metal induced by copper ions. *ACS Appl. Mater. Interfaces* 10, 22889–22895.
  24. Chen, S., Wang, H., Zhao, R., Rao, W., and Liu, J. (2020). Liquid metal composites. *Matter* 2, 1446–1480.
  25. Li, F., Shu, J., Zhang, L., Yang, N., Xie, J., Li, X., Cheng, L., Kuang, S., Tang, S., Zhang, S., et al. (2020). Liquid metal droplet robot. *Appl. Mater. Today* 19, 100597.
  26. Zhang, M., Yao, S., Rao, W., and Liu, J. (2019). Transformable soft liquid metal micro/nanomaterials. *Mat. Sci. Eng. R.* 138, 1–35.
  27. Daeneke, T., Khoshmanesh, K., Mahmood, N., Castro, I., Esrafilzadeh, D., Barrow, S., Dickey, M., and Kalantar-zadeh, K. (2018). Liquid metals: fundamentals and applications in chemistry. *Chem. Soc. Rev.* 47, 4073–4111.
  28. Zhang, W., Ou, J., Tang, S., Sivan, V., Yao, D., Latham, K., Khoshmanesh, K., Mitchell, A., Mullane, A., and Kalantar-zadeh, K. (2014). Liquid metal/metal oxide frameworks. *Adv. Funct. Mater.* 24, 3799–3807.
  29. Yi, L., and Liu, J. (2017). Liquid metal biomaterials: a newly emerging area to tackle modern biomedical challenges. *Int. Mater. Rev.* 62, 415–440.
  30. Chechetka, S., Yu, Y., Zhen, X., Pramanik, M., Pu, K., and Miyakoa, E. (2017). Light-driven liquid metal nanotransformers for biomedical theranostics. *Nat. Commun.* 8, 15432.
  31. Lu, Y., Hu, Q., Lin, Y., Pacardo, D., Wang, C., Sun, W., Ligler, F., Dickey, M., and Gu, Z. (2015). Transformable liquid-metal nanomedicine. *Nat. Commun.* 6, 10066.
  32. Lu, Y., Lin, Y., Chen, Z., Hu, Q., Liu, Y., Yu, S., Gao, W., Dickey, M., and Gu, Z. (2017). Enhanced endosomal escape by light-fueled liquid-metal transformer. *Nano Lett.* 17, 2138–2145.
  33. Sun, X., Cui, B., Yuan, B., Wang, X., Fan, L., Yu, D., He, Z., Sheng, L., Liu, J., and Lu, J. (2020). Liquid metal microparticles phase change mediated mechanical destruction for enhanced tumor cryoablation and dual-mode imaging. *Adv. Funct. Mater.* 30, 2003359.
  34. Varkouhi, A., Scholte, M., Storm, G., and Haisma, H. (2011). Endosomal escape pathways for delivery of biologicals. *J. Control Release* 151, 220–228.
  35. Qiu, C., Han, H., Sun, J., Zhang, H., Wei, W., Cui, S., Chen, X., Wang, J., and Zhang, Q. (2019). Regulating intracellular fate of siRNA by endoplasmic reticulum membrane-decorated hybrid nanoplexes. *Nat. Commun.* 10, 2702.
  36. Gong, N., Zhang, Y., Teng, X., Wang, Y., Huo, S., Qing, G., Ni, Q., Li, X., Wang, J., Ye, X., et al. (2020). Proton-driven transformable nanovaccine for cancer immunotherapy. *Nat. Nanotechnol.* 15, 1053–1064.
  37. Qiu, J., and Xia, Y. (2020). Killing cancer cells by rupturing their lysosomes. *Nat. Nanotechnol.* 15, 252–253.
  38. Kim, H., Lee, D., Kim, J., Kim, T., and Kim, W. (2013). Photothermally triggered cytosolic drug delivery via endosome disruption using a functionalized reduced graphene oxide. *ACS Nano* 7, 6735–6746.
  39. Shena, J., Chena, J., Ma, J., Fan, L., Zhang, X., Yue, T., Yan, Y., and Zhang, Y. (2020). Enhanced lysosome escape mediated by 1,2-dicarboxylic-cyclohexene anhydride-modified poly-L-lysine dendrimer as a gene delivery system. *Asian J. Pharm. Sci.* 15, 759–776.
  40. Martens, T., Remaut, K., Demeester, J., Smedt, S., and Braeckmans, K. (2014). Intracellular delivery of nanomaterials: how to catch endosomal escape in the act. *Nano Today* 9, 344–364.
  41. Wang, S., Liu, X., Chen, S., Liu, Z., Zhang, X., Liang, X., and Li, L. (2019). Regulation of Ca<sup>2+</sup> signaling for drug-resistant breast cancer therapy with mesoporous silica nanocapsule encapsulated doxorubicin/siRNA cocktail. *ACS Nano* 13, 274–283.
  42. Zhang, S., Gao, H., and Bao, G. (2015). Physical principles of nanoparticle cellular endocytosis. *ACS Nano* 9, 8655–8671.
  43. Fang, R., Hu, C., Luk, B., Gao, W., Copp, J., Tai, Y., O'Connor, D., and Zhang, L. (2014). Cancer cell membrane-coated nanoparticles for anticancer vaccination and drug delivery. *Nano Lett.* 14, 2181–2188.
  44. Jiang, Y., Krishnan, N., Zhou, J., Chekuri, S., Wei, X., Kroll, A., Yu, C., Duan, Y., Gao, W., Fang, R., et al. (2020). Engineered cell-membrane-coated nanoparticles directly present tumor antigens to promote anticancer immunity. *Adv. Mater.* 32, 2001808.
  45. Fang, R., Kroll, A., Gao, W., and Zhang, L. (2018). Cell membrane coating nanotechnology. *Adv. Mater.* 30, 1706759.
  46. Sun, H., Su, J., Meng, Q., Yin, Q., Chen, L., Gu, W., Zhang, P., Zhang, Z., Yu, H., Wang, S., et al. (2016). Cancer-cell-biomimetic nanoparticles for targeted therapy of homotypic tumors. *Adv. Mater.* 28, 9581–9588.
  47. Yu, B., Goel, S., Ni, D., Ellison, P., Siamof, C., Jiang, D., Cheng, L., Kang, L., Yu, F., Liu, Z., et al. (2018). Reassembly of <sup>69</sup>Zr-labeled cancer cell membranes into multicompartiment membrane-derived liposomes for PET-trackable tumor-targeted theranostics. *Adv. Mater.* 30, 1704934.
  48. Li, S., Xie, B., Cheng, H., Li, C., Zhang, M., Qiu, W., Liu, W., Wang, X., and Zhang, X. (2018). A biomimetic theranostic O<sub>2</sub>-meter for cancer targeted photodynamic therapy and phosphorescence imaging. *Biomaterials* 151, 1–12.
  49. Lv, Y., Liu, M., Zhang, Y., Wang, X., Zhang, F., Li, F., Bao, W., Wang, J., Zhang, Y., Wei, W., et al. (2018). Cancer cell membrane-biomimetic nanoprobes with two-photon excitation and near-infrared emission for intravital tumor fluorescence imaging. *ACS Nano* 12, 1350–1358.
  50. Wang, H., Yao, Y., He, Z., Rao, W., Hu, L., Chen, S., Lin, J., Gao, J., Zhang, P., Sun, X., et al. (2019). A highly stretchable liquid metal polymer as reversible transitional insulator and conductor. *Adv. Mater.* 31, 1901337.
  51. Chen, S., Wang, H., Sun, X., Wang, Q., Wang, X., Chen, L., Zhang, L., Guo, R., and Liu, J. (2019). Generalized way to make temperature

- tunable conductor-insulator transition liquid metal composites in a diverse range. *Mater. Horiz.* 6, 1854–1861.
52. Sun, X., Guo, R., Yuan, B., Chen, S., Wang, H., Dou, M., Liu, J., and He, Z. (2020). Low-temperature triggered shape transformation of liquid metal microdroplets. *ACS Appl. Mater. Interfaces* 12, 38386–38396.
53. Kurz, W., and Fisher, D.J. (1998). *Fundamentals of Solidification* (Forth Revised Edition) (Trans. Tech. Publications Ltd).
54. Meng, Q., Jiang, C., and Mao, S.X. (2007). Three-dimensional dendrite-like nanostructures of gallium nitride. *J. Cryst. Growth* 308, 166–169.
55. Penner, S., Stöger-Pollach, M., Klauser, F., Lorenz, H., Klötzer, B., Liu, X., Jenewein, B., and Bertel, E. (2009). Dendritic growth of amorphous gallium oxide in mixed GaOx/WOx thin films. *Mater. Chem. Phys.* 116, 175–182.
56. Wang, R., Yang, H., Fu, R., Su, Y., Lin, X., Jin, X., Du, W., Shan, X., and Huang, G. (2020). Biomimetic upconversion nanoparticles and gold nanoparticles for novel simultaneous dual-modal imaging-guided photothermal therapy of cancer. *Cancers* 12, 3136.
57. Glinsky, V., Glinsky, G., Glinskii, O., Huxley, V., Turk, J., Mossine, V., Deutscher, S., Pienta, K., and Quinn, T. (2003). Intravascular metastatic cancer cell homotypic aggregation at the sites of primary attachment to the endothelium. *Cancer Res.* 63, 3805–3811.
58. Hou, Y., Zhang, P., Wang, D., Liu, J., and Rao, W. (2020). Liquid metal hybrid platform-mediated ice–fire dual noninvasive conformable melanoma therapy. *ACS Appl. Mater. Inter.* 12, 27984–27993.
59. Hou, Y., Sun, X., Dou, M., Lu, C., Liu, J., and Rao, W. (2021). Cellulose nanocrystals facilitate needle-like ice crystal growth and modulate molecular targeted ice crystal nucleation. *Nano Lett.* 21, 4868–4877.
60. Baust, J., and Gage, A. (2005). The molecular basis of cryosurgery. *BJU Int.* 95, 1187–1191.
61. Morley, N., Burris, J., Cadwallader, L.C., and Nornberg, M.D. (2008). GalnSn usage in the research laboratory. *Rev. Sci. Instrum.* 79, 056107.
62. Han, X., Shen, S., Fan, Q., Chen, G., Archibong, E., Dotti, G., Liu, Z., Gu, Z., and Wang, C. (2019). Red blood cell-derived nanoerythrosome for antigen delivery with enhanced cancer immunotherapy. *Sci. Adv.* 5, eaaw6870.